Article:
Lu, Z., Bao, W., Wang, G. et al. (12 more authors) (2021) Mechanism of enhanced energy storage in AgNbO3-based lead-free antiferroelectrics. Nano Energy, 79. 105423. ISSN 2211-2855

https://doi.org/10.1016/j.nanoen.2020.105423

Nano Energy 79 (2021) 105423

Contents lists available at ScienceDirect

Nano Energy

journal homepage: http://www.elsevier.com/locate/nanoen

Mechanism of enhanced energy storage density in $AgNbO_3$-based lead-free antiferroelectrics

Zhilun Lu [a,b,1], Weichao Bao [c,1], Ge Wang [a,1], Shi-Kuan Sun [a,1], Linhao Li [a], Jinglei Li [d], Huijing Yang [a,e], Hongfen Ji [a,f], Antonio Feteira [g], Dejun Li [h], Fangfang Xu [c], Annette K. Kleppe [i], Dawei Wang [a,*], Shi-Yu Liu [h,*], Ian M. Reaney [a,*]

[a] Department of Materials Science and Engineering, University of Sheffield, Sheffield S1 3JD, UK
[b] The Henry Royce Institute, Sir Robert Hadfield Building, Sheffield S1 3JD, UK
[c] State Key Laboratory of High Performance Ceramics and Superfine Microstructure, Shanghai Institute of Ceramics, Shanghai 200050, China
[d] Electronic Materials Research Laboratory, Key Laboratory of the Ministry of Education and International Center for Dielectric Research, Xi'an Jiaotong University, Xi'an 710049, Shaanxi, China
[e] Department of Physics, Tangshan Normal University, Tangshan 063000, China
[f] Laboratory of Thin Film Techniques and Optical Test, Xi'an Technological University, Xi'an 710032, China
[g] Materials and Engineering Research Institute, Sheffield Hallam University, Sheffield S1 1WB, UK
[h] College of Physics and Materials Science, Tianjin Normal University, Tianjin 300387, China
[i] Diamond Light Source Ltd, Harwell Science and Innovation Campus, Didcot OX11 0DE, UK

ARTICLE INFO

Keywords:
Energy storage capacitors
Antiferroelectrics
In-situ synchrotron X-ray diffraction
Silver niobate

ABSTRACT

The mechanisms underpinning high energy storage density in lead-free $Ag_{1-3x}Nd_xTa_yNb_{1-y}O_3$ antiferroelectric (AFE) ceramics have been investigated. Rietveld refinements of in-situ synchrotron X-ray data reveal that the structure remains quadrupled and orthorhombic under electric field (E) but adopts a non-centrosymmetric space group, $Pmc2_1$, in which the cations exhibit a ferrielectric configuration. Nd and Ta doping both stabilize the AFE structure, thereby increasing the AFE-ferrielectric switching field from 150 to 350 kV cm^{-1}. Domain size and correlation length of AFE/ferrielectric coupling reduce with Nd doping, leading to slimmer hysteresis loops. The maximum polarization (P_{max}) is optimized through A-site aliovalent doping which also decreases electrical conductivity, permitting the application of a larger E. These effects combine to enhance energy storage density to give W_{rec} = 6.5 J cm^{-3} for $Ag_{0.97}Nd_{0.01}Ta_{0.20}Nb_{0.80}O_3$.

1. Introduction

Dielectric capacitors have attracted interest for pulsed power applications due to their high power densities and fast charge-discharge rates [1,2] but their low energy storage densities have restricted their use [3]. For a dielectric capacitor, the total energy density (W), recoverable energy density (W_{rec}), energy storage efficiency (η) and the energy loss (W_{loss}) are:

$$W = \int_0^{P_{max}} EdP, \quad (1)$$

$$W_{rec} = \int_{P_r}^{P_{max}} EdP, \quad (2)$$

$$\eta = W_{rec}/W, \quad (3)$$

$$W_{loss} = W - W_{rec}, \quad (4)$$

Antiferroelectric (AFE) ceramics are promising candidates for high energy density due to their large P_{max} and small remanent polarization (P_r) [4]. Extensive research has been carried out on lead-based AFEs over the last decade [5,6] (e.g. lead lanthanum zirconium titanate), due to their high W_{rec} ~6.4 J cm^{-3} [7] but their toxicity drives an environmental and commercial need for lead-free equivalents [8]. Recently, many studies have focused on lead-free relaxor-type ceramic dielectrics

* Corresponding authors.
E-mail addresses: dawei.wang@sheffield.ac.uk (D. Wang), shiyuliu@mail.tjnu.edu.cn (S.-Y. Liu), i.m.reaney@sheffield.ac.uk (I.M. Reaney).
[1] Z. Lu, W. Bao, G. Wang and S. Sun contributed equally to this work.

https://doi.org/10.1016/j.nanoen.2020.105423
Received 31 July 2020; Received in revised form 1 September 2020; Accepted 19 September 2020
Available online 30 September 2020

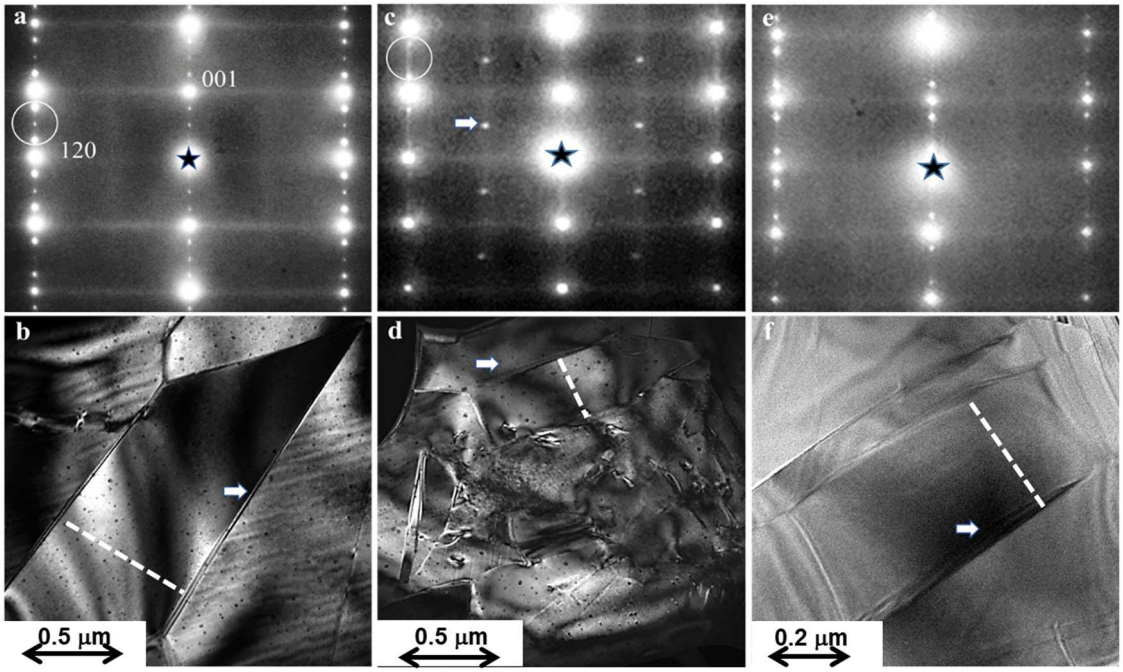

Fig. 1. $[210]_c$ (c = cubic) zone axis diffraction patterns and corresponding dark field images obtained using (001) reflections from a) and b) $AgNbO_3$ and c) and d) $Ag_{0.91}Nd_{0.03}NbO_3$. The arrowed reflections at $(^1/_2 1^1/_2)_c$ in c are contaminant from a second $[102]_c$ domain. The circles in a and c highlight elongation and streaking of the $\pm$ ¼$\{00l\}_c$ reflections as Nd increases. e) $[210]_c$ zone axis diffraction pattern of $Ag_{0.97}Nd_{0.01}Ta_{0.20}Nb_{0.80}O_3$. f) Bright field TEM image of domains in a grain of $Ag_{0.97}Nd_{0.01}Ta_{0.20}Nb_{0.80}O_3$. To aid the reader, domain walls (arrows) and widths (dashed lines) are indicated in the images.

based on, e.g. $Na_{0.5}Bi_{0.5}TiO_3$, $BaTiO_3$ and $BiFeO_3$ [9–13]. Generally, these materials offer promising properties at $E > 500$ kV cm^{-1} in multilayer ceramic capacitors (MLCCs) with dielectric layer thickness < 10 μm. Lead free AFE ceramics, such as $AgNbO_3$, also offer the potential of high energy density due to the delayed onset of an AFE-ferroelectric transition but optimum properties are typically achieved at lower E than relaxors (<500 kV cm^{-1}) [14].

$AgNbO_3$ has the prototype perovskite structure but exhibits a complex sequence of phase transitions on cooling, Table S1 [15,16]. In 2016, Zhao et al. [17] demonstrated that MnO_2 increased W_{rec}, which the authors ascribed to enhanced AFE stability, prompting several further studies [18–22]. W_{rec} of 2.6 J cm^{-3} was obtained for Bi-doped $AgNbO_3$ and Ca-doped $AgNbO_3$ achieved W_{rec} = 3.55 J cm^{-3}, which was attributed to enhanced breakdown strength (BDS), smaller grain size, Ag vacancies and a reduced tolerance factor (t) [18,21]. W_{rec} of 4.4 J cm^{-3} and 4.5 J cm^{-3} were attained for La and Gd doped $AgNbO_3$ ceramics, respectively [19,22], with the authors quoting similar reasons to those in references [17,20]. The assertion that decreasing t increases AFE stability has been stated by several other researchers [23,24], but W and Ta doping, which lower B-site polarizability but not t, also enhance AFE stability, giving W_{rec} of 3.3 J cm^{-3} and 4.2 J cm^{-3}, respectively [25–27].

This brief review highlights several factors that optimize energy storage performance in $AgNbO_3$ ceramics [17–22,25–27] but there is only limited evidence of the underlying mechanisms. We have therefore, studied the energy storage properties and crystal chemistry of $Ag_{1-3x}Nd_xNbO_3$ and $Ag_{0.97}Nd_{0.01}Ta_yNb_{1-y}O_3$ ($x = 0.00$, 0.01, 0.02 and 0.03; $y = 0.10$, 0.15, 0.20 and 0.25) ceramics in which W_{rec} of 6.5 J cm^{-3} and η of 71%, were obtained for $Ag_{0.97}Nd_{0.01}Ta_{0.20}Nb_{0.80}O_3$ at 370 kV cm^{-1}.

2. Experimental

$Ag_{1-3x}Nd_xNbO_3$ and $Ag_{0.97}Nd_{0.01}Ta_yNb_{1-y}O_3$ ($x = 0.00$, 0.01, 0.02 and 0.03; $y = 0.10$, 0.15, 0.20 and 0.25) ceramics were fabricated by solid state reaction using Ag_2O (>99%, Acros Organics), Nd_2O_3 (>99.9%, Sigma-Aldrich), Nb_2O_5 (>99.99%, Sigma-Aldrich) and Ta_2O_5 (>99.9%, Stanford Materials Corporation) powders. Stoichiometric amounts of dry raw powders were weighed and ball-milled 12 h using Y_2O_3-stabilized ZrO_2 as grinding media in isopropanol. The mixed powders were dried, calcined 6 h at 900 °C in oxygen and then ball-milled 6 h. The dry powders were uniaxially pressed into 8 mm diameter pellets then sintered 4 h at 1100-1150 °C in oxygen. Densities of sintered ceramics were measured using the Archimedes method and were typically ~95% of the theoretical value.

X-ray diffraction (XRD) on ceramic samples was performed using a Bruker D2 phaser benchtop system. The surface morphology of thermally etched polished samples was examined using a FEI Inspect F50 scanning electron microscope (SEM) with a backscattered electron (BSE) detector. Thermal etching of polished samples was conducted at 90% of the sintering temperature for 20 min. Samples for transmission electron microscopy (TEM) were ground manually to a thickness of ~50 μm using a SiC slurry. Ion thinning was conducted at 0.5–3 kV using an Ar ion mill set at an incidence angle of 6° (PIPS II 695, Gatan, USA). TEM images and electron diffraction patterns were acquired using a JEOL JEM 2100F (Tokyo, Japan) operated at 200 kV.

In-situ high-energy synchrotron XRD experiments were performed at the I15 Diamond light source with a photon energy of 72 keV (λ=0.1722 Å). Ceramic samples were cut into rectangular bars (L5.0 × W1.0 × T0.2 mm), annealed 2 h at 800 °C to eliminate residual stresses and sputter coated with Au to form electrode (area of L4.0 × W0.8 mm) on top and bottom surface. The bar-shaped samples were placed in silicone oil in a custom-designed polyimide holder. During in-situ experiments, the sample holder was electrically connected to a high voltage amplifier (Matsusada EC-10). The X-ray beam was focused and collimated to 70 μm diameter. Transmission and 2-D diffraction patterns were collected using Pilatus 2M detector located ~1 m downstream of the sample prior, during and after application of external E. Collected XRD patterns were calibrated, integrated to eliminate the texture effect and converted into conventional one-dimensional XRD patterns using Dawn software. Full-pattern Rietveld refinements were conducted using Topas 6 software to obtain

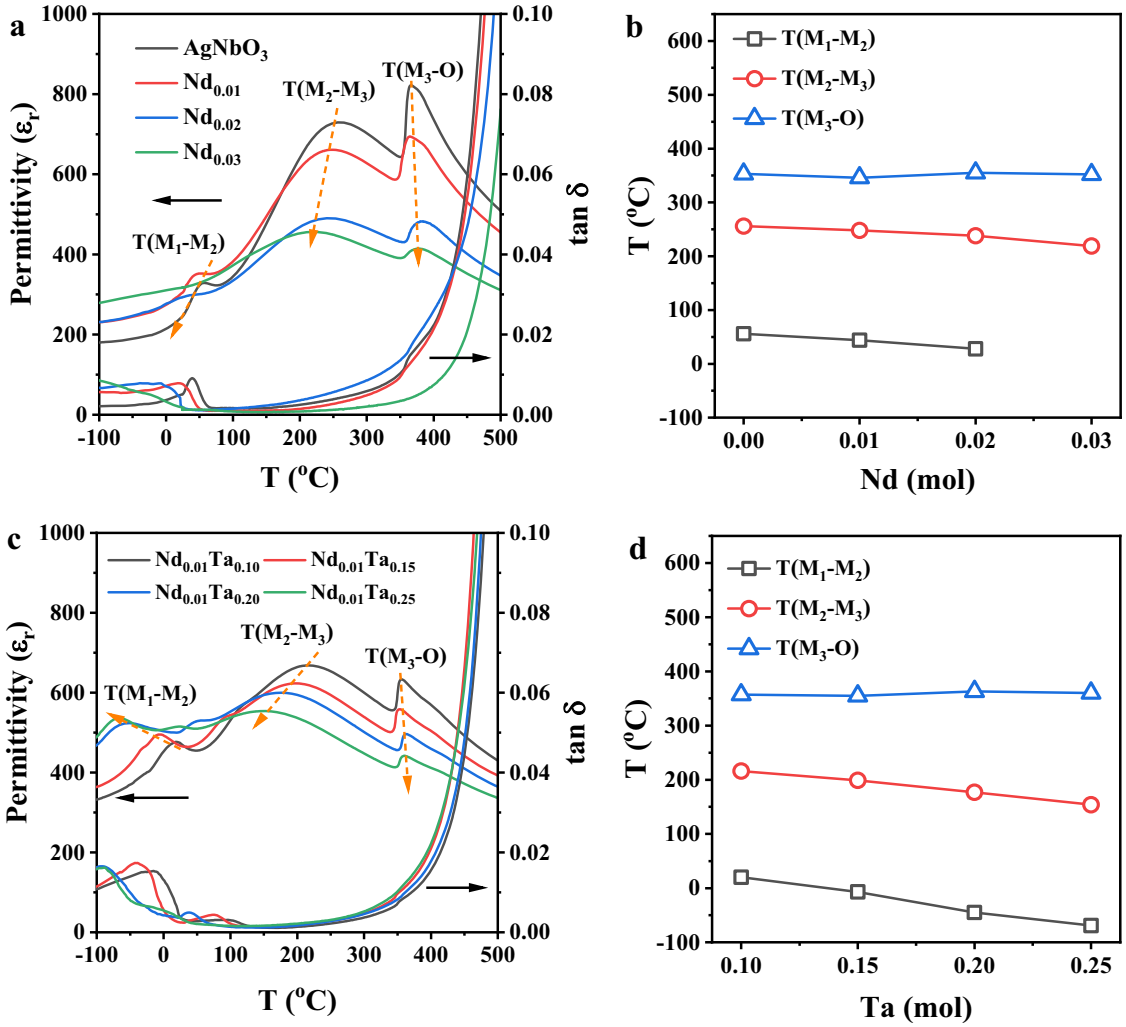

Fig. 2. The temperature dependence of dielectric permittivity (ε_r vs T) and loss (tanδ vs T) at 100 kHz and phase transition temperatures based on the temperature dependence of dielectric permittivity of a, b, $Ag_{1-3x}Nd_xNbO_3$ and c, d, $Ag_{0.97}Nd_{0.01}Ta_yNb_{1-y}O_3$ ceramics. M_1: ferroelectric, M_2: disordered AFE, M_3: disordered AFE, and O: paraelectric.

crystallographic information.

Impedance spectroscopy (IS) data were collected using an Agilent E4980A (Agilent Technologies Inc., Palo-Alto, CA) from 20 Hz to 2 MHz and from 400 to 600 °C at 100 mV. Resistivity was obtained by fitting the experimental data using ZView software (Scribner Associates, Inc., Southern Pines, NC). Temperature dependence of dielectric properties was measured using an Agilent 4184A precision LCR meter from room temperature (RT) to 600 °C at 1, 10, 100, 250 kHz and 1 MHz. IS and LCR data were corrected by a geometric factor (thickness/surface area). To obtain polarization-field (P-E) loops, ceramic samples were ground to ~0.15 mm and gold sputtered to give a circular electrode with an area of 7 mm^2. Bipolar P-E loops were obtained using an aixACCT TF 2000E ferroelectric tester at 1 Hz.

3. Results and discussions

All peaks in XRD patterns (Fig. S1) were indexed according to a single orthorhombic perovskite structure with *Pbcm* symmetry. An enlarged view of the $\{200\}_c$ peak (Fig. S1a) illustrates that splitting decreases with increasing Nd concentration. As Ta concentration increases however, a reduction in splitting is also accompanied by peaks shifting to higher 2θ values (Fig. S1b), suggesting smaller d-spacings. Ta^{5+} and Nb^{5+} have the same effective ionic radius (0.64 Å, CN = 6) [28] and it is most likely the decrease in ionic polarizability from Nb to Ta which reduces the average off-centering of the B-site ion in the octahedra and modifies the cell parameters [23].

SEM images of thermally-etched polished ceramic samples are shown in Fig. S2, which reveal equiaxed grains with minimal porosity, consistent with a relative density ~95%. The average grain size of all studied samples was < 5 μm, with the smallest (~2 μm) in $x = 0.02$. Nd doping with $x = 0.01$ and 0.02 inhibits grain growth but for $x \geq 0.03$, the grain size increases, and secondary phases emerge. The grain size increases from ~2.5 μm in $Nd_{0.01}$ to ~5 μm in $Nd_{0.01}Ta_{0.10}$ as a result of the higher sintering temperature employed for the latter. The average grain size decreases slightly with further increasing Ta concentration (Fig. S2e–h), which may be associated with the more refractory nature of Ta_2O_5 in comparison with Nb_2O_5 [29].

Fig. 1a–d shows $[210]_c$ (c = cubic) zone axis electron diffraction patterns and the corresponding dark field images obtained using fundamental $(001)_c$ perovskite reflections for $Ag_{1-3x}Nd_xNbO_3$ compositions. As Nd concentration increases to 0.03, the domain width decreases from ~1 μm (Fig. 1b) to < 0.3 μm (Fig. 1d) which is attributed to disruption of the antipolar order due to the presence of $Nd_{Ag}^{\cdot\cdot}$ and $V_{Ag}^{'}$. The disruption in antipolar order is also manifest in electron diffraction patterns as elongation and streaking of the ± ¼$\{00l\}_c$ reflections in the $[001]_c$ direction as x increases from 0 (Fig. 1a) to 0.03 (Fig. 1c). The streaking (highlighted by circles in Fig. 1a and c) and decrease in domain width (highlighted by dashed lines in Fig. 1b and d) are

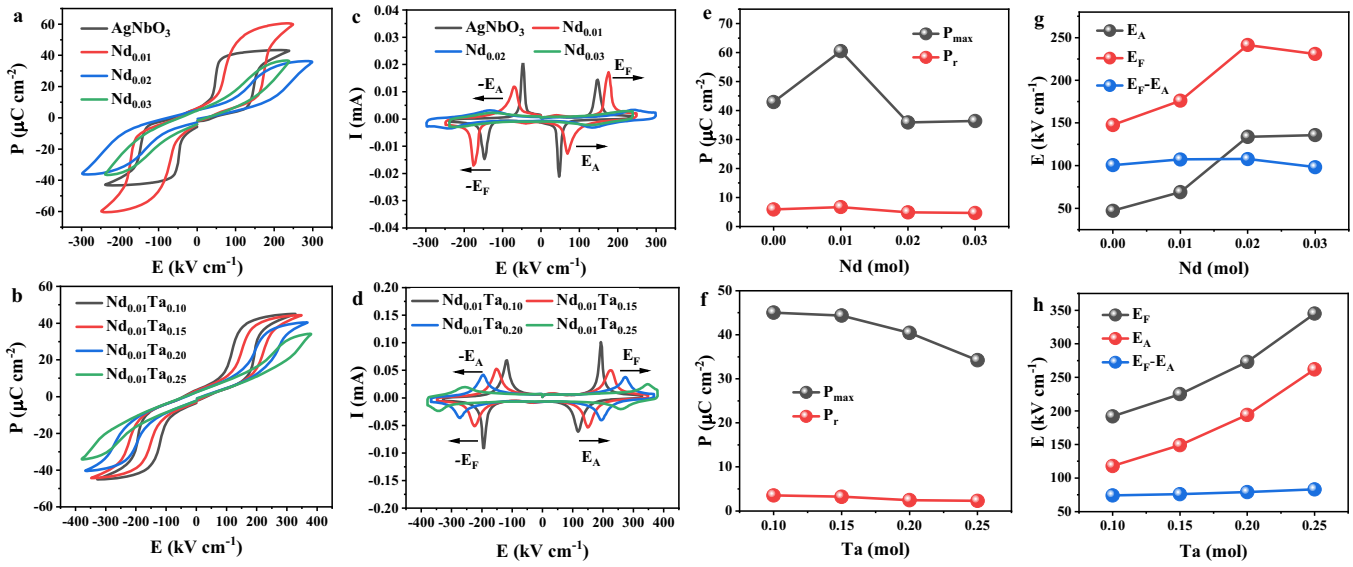

Fig. 3. Compositional variation of antiferroelectric properties under maximum electrical fields: a, b, P-E loops; c, d, I-E curves; e, f, Changes of P_{max} and P_r; g, h, Changes of E_F, E_A; and E_F-E_A, as a function of Nd and Ta concentration.

consistent with the reduction in splitting of the $\{200\}_c$ peaks in XRD patterns as x increases, Fig. S1. Although these images and patterns are recorded at zero-field, we anticipate that partial disruption in long range coupling, related to the presence on $Nd_{Ag}^{\cdot\cdot}$ and $V_{Ag}^{'}$, is maintained in the field induced phase. A $[210]_c$ diffraction pattern and its associated bright field image for $Ag_{0.97}Nd_{0.01}Ta_{0.20}Nb_{0.80}O_3$ are shown in Fig. 1e and f, respectively. Ta doping qualitatively reduces the intensity of the ¼$\{00l\}_c$ peaks (Fig. 1e) but the disruption of the antipolar coupling (streaking in electron diffraction patterns) is less apparent in comparison to Fig. 1c ($x = 0.03$) since the concentration of Nd is lower ($x = 0.01$). The nanoparticles (dark spots) observed throughout the TEM images are composed of Ag and are artifacts of the ion thinning process.

Typical Z* plots, combined Z" and M" spectroscopic plots, and Arrhenius plots of $Ag_{1-3x}Nd_xNbO_3$ and $Ag_{0.97}Nd_{0.01}Ta_yNb_{1-y}O_3$ ceramics are given in Fig. S3. Only one semicircle was observed in the Z* plot for all compositions, as shown in Fig. S3a and b, and one Debye peak in both Z" and M" spectroscopic plots locates at the same frequency (Fig. S3c and d), indicating that all samples are electrically homogeneous [30]. The total resistivity of the ceramics (obtained from low frequency intercepts in Z* plots) increases with increasing Nd and/or Ta concentration, together with an increase in activation energy (Fig. S3e and f), suggesting potential enhancement of BDS [31].

The temperature dependence of permittivity (ε_r vs T) and loss ($\tan\delta$ vs T) at 100 kHz of $Ag_{1-3x}Nd_xNbO_3$ and $Ag_{0.97}Nd_{0.01}Ta_yNb_{1-y}O_3$ ceramics are shown in Fig. 2. A sequence of dielectric anomalies is

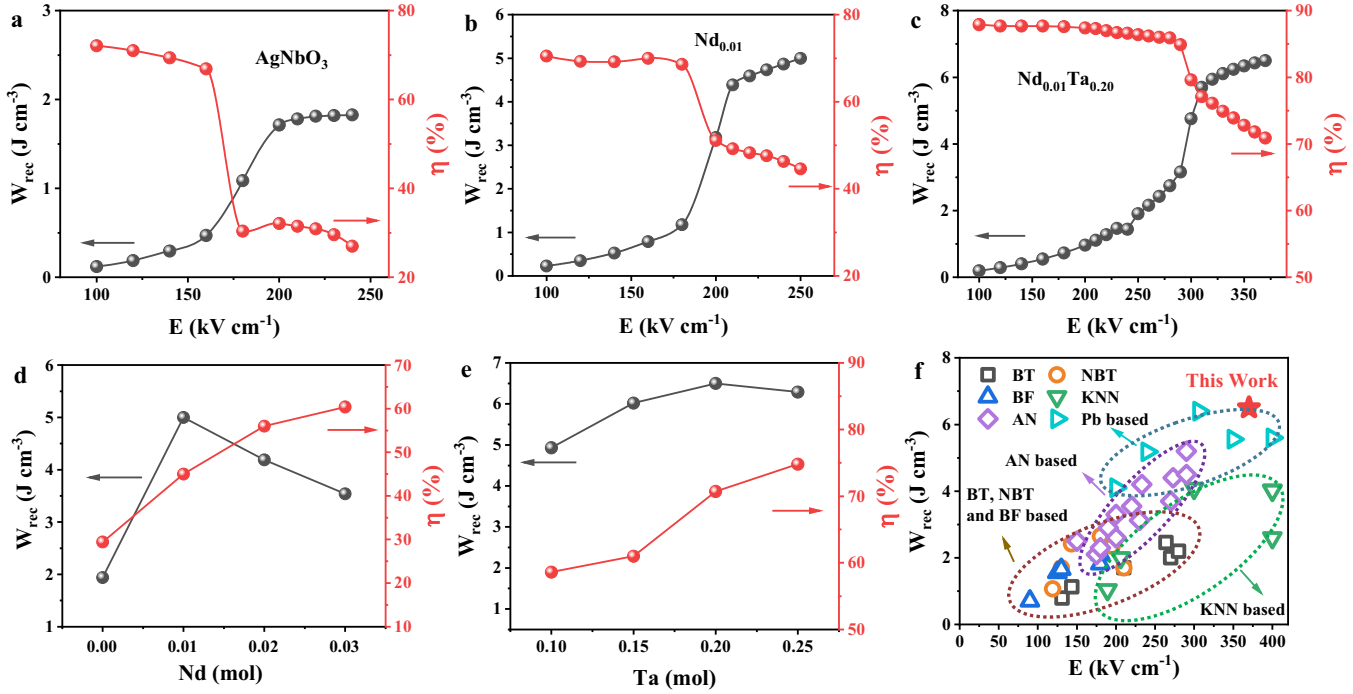

Fig. 4. W_{rec} and η of a, $AgNbO_3$; b, $Ag_{0.97}Nd_{0.01}NbO_3$; c, $Ag_{0.97}Nd_{0.01}Ta_{0.20}Nb_{0.80}O_3$ under the respective E. d, e, W_{rec}, and η as a function of Nd and Ta content in this work. f, a comparison of W_{rec} of $Ag_{0.97}Nd_{0.01}Ta_{0.20}Nb_{0.80}O_3$ ceramics among other lead-free bulk ceramics [7,10,17–19,21,22,25–27,31,33–64].

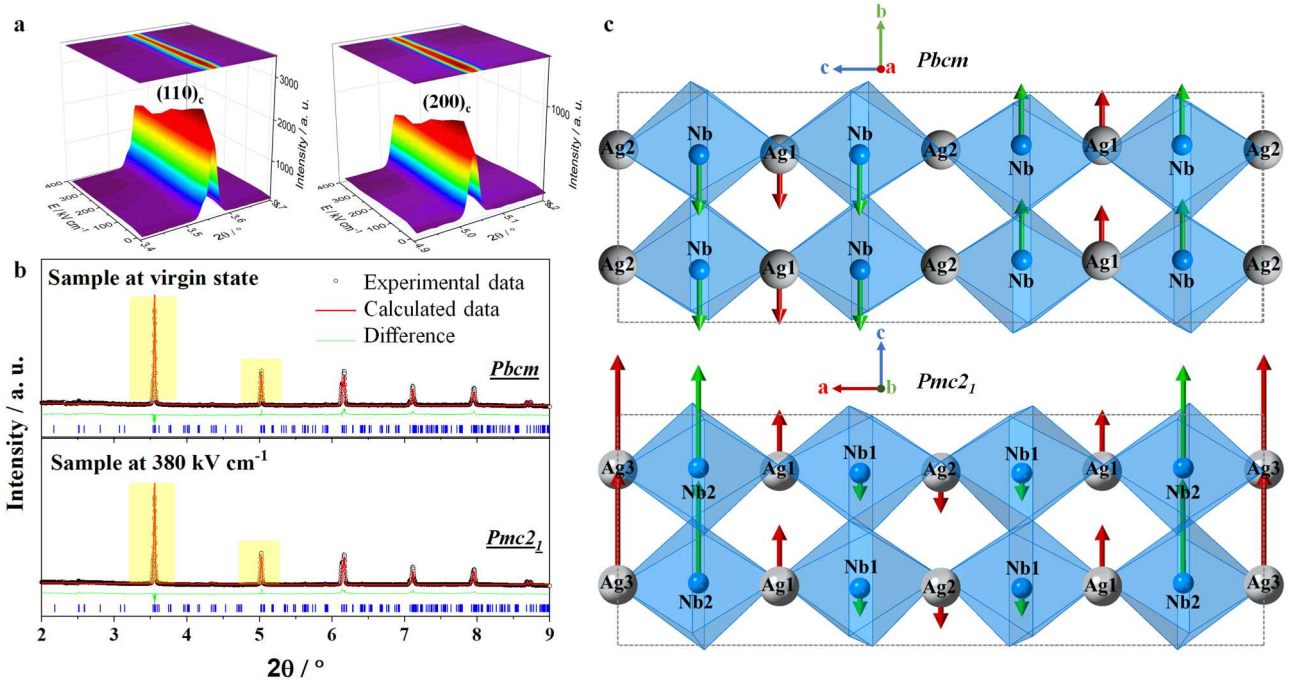

Fig. 5. a) The changes of XRD representative peaks of $(110)_c$ and $(200)_c$ (c = cubic) during application of E up to 380 kV cm^{-1}; b) Rietveld refinement of high energy synchrotron XRD patterns of $Ag_{0.97}Nd_{0.01}Ta_{0.25}Nb_{0.75}O_3$ ceramic at zero field and 380 kV cm^{-1} (above E_F) with the shaded peaks corresponding a) and c) schematics of the displacements in the unit cell. Red and green arrows are the relative displacements along the *b*-axis in *Pbcm* (equivalent to the *c*-axis in *Pmc2$_1$*) of Ag^+ and Nb^{5+} ions, respectively, from the center positions. (For interpretation of the references to color in this figure legend, the reader is referred to the web version of this article.)

observed, consistent with the phase transitions reported for undoped $AgNbO_3$ (Table S1) [16]. Dielectric anomalies around 50 °C, 250 °C and 350 °C were assigned to the M_1-M_2, M_2-M_3 and M_3-O phase transitions, respectively. The M_3-O phase transition temperature is unaffected by dopant concentration but as x increases, the M_2-M_3 dielectric anomalies shift to lower temperature. The same effect is seen for the M_1-M_2 transition for $x \leq 0.02$. However, for $Nd_{0.03}$, the M_1-M_2 transition could not be observed even at −100 °C in contrast to previous reports which have speculated that the M_1-M_2 phase transition simply shifts to below room temperature [32]. Ta doping leads to similar temperature dependence of dielectric anomalies associated with M_1-M_2 and M_2-M_3 phase transitions, as shown in Fig. 2b and d, with all M_1-M_2 transitions for $Ag_{0.97}Nd_{0.01}Ta_yNb_{1-y}O_3$ ceramics > 25 °C. For Nd doped and Nd/Ta co-doped $AgNbO_3$ samples, the temperature dependence of dielectric loss shows a maximum in the vicinity of the M_1-M_2 phase transition, a very small anomaly related to the M_3-O phase transition and no anomaly for the M_2-M_3 phase transition. The frequency dependent permittivity (ε_r vs T) and loss (tanδ vs T) for the Nd/Ta co-doped samples are presented in Fig. S4, suggesting that the M_2-M_3 phase transition is frequency independent.

P-E and current-electric field (I-E) loops as a function of composition under maximum applied field (E_{max}) for $Ag_{1-3x}Nd_xNbO_3$ and $Ag_{0.97}Nd_{0.01}Ta_yNb_{1-y}O_3$ ceramics are shown in Fig. 3a–d. All compositions exhibit double hysteresis loops, typical AFE behavior. For Nd doped samples (Fig. 3a), E_{max} increases with Nd concentration to 300 kV cm^{-1} for $Nd_{0.02}$ and then decreases to 240 kV cm^{-1} for $Nd_{0.03}$ possibly due to the presence of secondary phases, Fig. S2i. The variation of E_{max} as a function of Nd concentration is consistent with IS data and SEM images and contiguous with a reduced grain size and increased resistivity each of which has been reported to enhance dielectric BDS [33,34].

As Nd concentration increases, P_{max} and P_r first increase ($Nd_{0.01}$) but then decrease for $x > 0.01$, as shown in Fig. 3e. The antipolar to polar switching field may be used to estimate the AFE phase stability. The dependence of the forward switching field (E_F), the backward switching field (E_A) and its difference (E_F-E_A) are shown as a function of Nd concentration in Fig. 3g. E_F increases from 147 kV cm^{-1} for $AgNbO_3$ to 241 kV cm^{-1} for $Nd_{0.02}$ but decreases for $Nd_{0.03}$, presumably due to the presence of secondary phases, Fig. S2i. E_A increases from 47 to 136 kV cm^{-1} for $AgNbO_3$ and $Nd_{0.03}$, respectively. The increase in E_F and E_A suggests that Nd stabilizes the antipolar with respect to polar phase.

For Ta doped samples, P_{max} and P_r decrease since the polarizability of Ta is lower than Nb [25], but the increase in P_{max} for $x = 0.01$ in the $Ag_{1-3x}Nd_xNbO_3$ solid solution series suggests that it is already optimized, as shown in Fig. 3f. E_F and E_A increase with Ta concentration establishing that the antipolar is stabilized with respect to the polar phase at zero field, Fig. 3h.

Fig. 4a–c show representative energy storage properties of $Ag_{1-3x}Nd_xNbO_3$ and $Ag_{0.97}Nd_{0.01}Ta_yNb_{1-y}O_3$ ceramics at different E with data from further compositions shown in Fig. S5. The corresponding P-E loops are presented in Fig. S6. Generally, η decreases and W_{rec} increases with the increasing E. W_{rec} however, reaches a maximum of 6.5 J cm^{-3} at 370 kV cm^{-1} with η of 71% for $Ag_{0.97}Nd_{0.01}Ta_{0.20}Nb_{0.80}O_3$, decreasing slightly at higher Ta concentrations. These values are superior or equivalent to current lead-free AFE ceramics, Fig. 4f and the reported values of the commercial lead-based incumbents [7,10,17–19,21,22,25–27,31,33–64].

In-situ synchrotron XRD was employed to study the crystal structure of $Ag_{0.97}Nd_{0.01}Ta_{0.25}Nb_{0.75}O_3$ ceramics prior, during and after application of E. This composition has the highest BDS from Fig. 3b and was thus least likely to breakdown during in-situ poling experiment.

Fig. 5a shows the effect of E on a) two XRD representative peaks (indexed using cubic prototype cell); b) illustrates the full-pattern refinements of the zero-field and field-induced phases and c) reveals the schematic structures at zero field and 380 kV cm^{-1} in which the relative ion displacements are represented as arrows. The best refinement of AFE phase at zero field was obtained using orthorhombic *Pbcm* symmetry with Goodness of Fit (GoF) = 1.07, however, small changes in the intensity of the peaks were observed (Fig. 5a) at 380 kV cm^{-1} (above E_F). Several symmetries were used to try and refine XRD patterns under field, including *Pbcm* (orthorhombic, space group 57, GoF = 1.10) but *Pmc2$_1$*

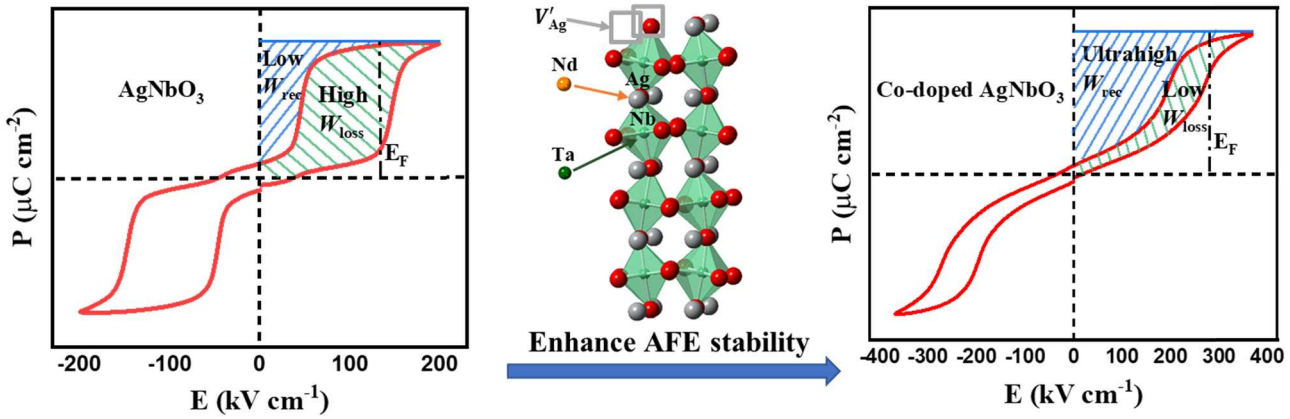

Fig. 6. Schematic diagram illustrating how W_{rec} is optimized through doping in $AgNbO_3$. Gray, yellow, green, dark green and red spheres represent Ag, Nd, Nb, Ta and O atoms, respectively. Gray squares represent silver vacancies. (For interpretation of the references to color in this figure legend, the reader is referred to the web version of this article.)

(orthorhombic, space group 26, GoF = 1.02) provided a marginally better description of the symmetry compared with the others, as shown in Fig. 5b. We note however, in *Pbcm*, the long axis is *c* (≈4a_c, where a_c is cubic perovskite cell parameter) but in $Pmc2_1$, *a* has the largest lattice parameter. The refinement parameters are listed in Table S2. Given the marginally better GOF and that P-E loops open and exhibit hysteresis above a threshold value, E_F, we conclude that the noncentrosymmetric, $Pmc2_1$ space group best describes the symmetry of $Ag_{0.97}Nd_{0.01}Ta_{0.25}Nb_{0.75}O_3$ at 380 kV cm^{-1}. Fig. 5c shows schematics of the zero field and field induced structures with $b_{Pbcm}//c_{Pmc21}$, emphasizing the relative cation displacements (arrows) and how they differ in the centro- (*Pbcm*) and noncentrosymmetric ($Pmc2_1$) space groups, In the centrosymmetric *Pbcm* cell, Ag and Nb atoms averagely displace ± 0.019 and ± 0.021 Å along the *b* axis, respectively whereas the average displacements are estimated to be 0.041 and 0.008 Å for (Ag, Nd) and (Nb, Ta) in the field induced $Pmc2_1$ cell along the *c* axis (equivalent to *b* in *Pbcm*). In the *Pbcm* cell, the Ag2 sites do not displace whereas the Ag1 sites have equal antiparallel displacements along [010]/[0$\bar{1}$0], Fig. 5c. Similarly, in the *Pbcm* cell, the Nb/Ta sites displace equally along [010]/[0$\bar{1}$0] in antiparallel. In contrast, Ag3 ions in the $Pmc2_1$ cell (equivalent to outer Ag2 ions in the schematic of the *Pbcm* cell) exhibit a parallel displacement along [001], Ag1 sites in $Pmc2_1$ displace in parallel along [001] with Ag2 in antiparallel with Ag1 and 3 along [00$\bar{1}$]. The Ag sub-lattice therefore, exhibits a net polarization along the *c* axis (equivalent to the *b* axis in the *Pbcm* setting). The four pairs of Nb^{5+}/Ta^{5+} ions exhibit unequal antiparallel displacements along [001]/[00$\bar{1}$] to give a further net contribution to polarization along the *c* axis. The field-induced transition may therefore, be considered to occur between a quadrupled, orthorhombic AFE to a ferrielectric phase whose average structure does not involve a change in crystal class or in the number of perovskite formula units per unit cell. In contrast, in $Pb(Zr,Ti)O_3$ (PZT)-based AFE materials, a rhombohedral polar structure is stabilized at high field which involves a change in crystal class and a large strain (0.45% at 60 kV cm^{-1}) [65]. The total strain for $Ag_{0.97}Nd_{0.1}Ta_{0.25}Nb_{0.75}O_3$ was calculated as 0.06% at 380 kV cm^{-1} from representative reflections in in-situ XRD data using the Daymond method [12].

To explore further the microscopic origin of energy storage properties in Nd/Ta co-doped $AgNbO_3$ lead-free AFE ceramics, first-principles density functional theory (DFT) calculations and Landau–Ginzburg–Devonshire (LGD) phenomenological theory were carried out. The detailed information can be obtained in Fig. S7 (supplementary information) but in summary, preliminary DFT calculations and LGD phenomenological theory both concur that Nd/Ta co-doping stablizes the AFE structure, thereby increasing the field required for the onset of the AFE-ferrielectric induced phase transition.

From the above results and discussion, there are a number of critical factors that lead to the optimization of W_{rec} in Nd/Ta co-doped $AgNbO_3$:

i) Nd and Ta increase the resistivity of bulk $AgNbO_3$, which coupled with the absence of easy pathways for conduction, permits the application of larger *E* prior to breakdown. Larger *E* favors high P_{max} and therefore a greater area to the left of the P-E loop in the positive quadrant.
ii) $Nd_{Ag}^{\cdot\cdot}$ and their associated $V_{Ag}^{'}$ on the A-site optimize P_{max}.
iii) The presence of $Nd_{Ag}^{\cdot\cdot}$ and $V_{Ag}^{'}$ decreases long-range coupling of antipolar and thereby induced ferrielectric order. This effect is manifested in a reduction of splitting in $\{200\}_c$ peaks in XRD patterns, smaller AFE domains and streaking of ± ¼$\{00l\}_c$ reflections in electron diffraction patterns, respectively, as Nd concentration increases. The induced ferrielectric portion of the P-E loop becomes slimmer and the area to its left increases.
iv) Nd and Ta increase the stability of the AFE phase. Enhanced AFE stability increases E_F and improves W_{rec} by increasing the area to the left of the P-E loop.

Nd/Ta co-doping in $AgNbO_3$ thus create a set of crystallo-chemical criteria which in combination optimize W_{rec}. Importantly, the AFE to ferrielectric transition does not involve a change in crystal class so potentially offers minimum strain (0.06% at 380 kV cm^{-1}) in comparison with lead-based analogs such La doped PZT (0.71% at 300 kV cm^{-1}) [66]. We note that enhancement of W_{rec} for lead-free relaxors has been reported for films and multilayers with respect to ceramics due to the larger BDS [9,67]. It remains to be elucidated whether multilayers of Nd/Ta co-doped $AgNbO_3$ achieve a similar enhancement with respect to bulk ceramic properties. A schematic illustrating how these principles combine to optimize W_{rec} is shown in Fig. 6.

4. Conclusions

In summary, W_{rec} of 6.5 J cm^{-3}, equivalent to lead-based ceramics, was achieved in $Ag_{0.97}Nd_{0.01}Ta_{0.20}Nb_{0.80}O_3$, at an applied *E* of 370 kV cm^{-1}. The factors which result in such a large W_{rec} in Nd/Ta co-doped $AgNbO_3$ are complex but are ascribed to four key points: (i) an increase in resistivity which increases BDS and permits the application of larger *E*, (ii) optimization of P_{max} through A-site aliovalent doping, (iii) slimmer portion of the P-E loop in the induced ferrielectric region due to the presence of $Nd_{Ag}^{\cdot\cdot}$ and $V_{Ag}^{'}$ defects, and iv) stabilization of the AFE phase, giving higher E_F.

CRediT authorship contribution statement

D.W., S.L., and I.M.R. supervised the research. Z.L. wrote the article and carried out the electrical and energy storage property. Z.L., G.W., L. L., D.W. and A.K.K. contributed to the in-situ synchrotron X-ray experiment. S.S. conducted the SEM characterizations. W.B. and F.X. conducted the TEM characterizations. J.L., H.Y., H.J. and A.F. contributed to data discussion and to write the article. D.L. and S.L. developed the theory and performed the computations. All the authors discussed the results and commented on the manuscript.

Declaration of Competing Interest

The authors declare that they have no known competing financial interests or personal relationships that could have appeared to influence the work reported in this paper.

Acknowledgments

We wish to acknowledge the Henry Royce Institute for Advanced Materials, funded through the Engineering and Physical Sciences Research Council (EPSRC) grants EP/R00661X/1, EP/S019367/1, EP/P02470X/1 and EP/P025285/1, for the financial support at The University of Sheffield. We thank the Science and Technology Program of Guangzhou (Grant No. 201704030095) and EPSRC for funding (Substitution and Sustainability in Functional Materials and Devices, EP/L017563/1, Synthesizing 3D Metamaterials for RF, microwave and THz applications, EP/N010493/1, FPeT: Framework for designing piezoelectric transformer power supplies, EP/P015859/1) and support provided by Functional Materials and Devices group from The University of Sheffield. Additionally, we thank David A. Hall (University of Manchester) for assitance with sample preparation and Diamond Light Source for access to beamline I15 (proposal number CY21714-3) that contributed to the results presented here.

Appendix A. Supporting information

Supplementary data associated with this article can be found in the online version at doi:10.1016/j.nanoen.2020.105423.

References

[1] B. Chu, X. Zhou, K. Ren, B. Neese, M. Lin, Q. Wang, F. Bauer, Q.M. Zhang, A dielectric polymer with high electric energy density and fast discharge speed, Science 313 (2006) 334–336.
[2] Z. Sun, Z. Wang, Y. Tian, G. Wang, W. Wang, M. Yang, X. Wang, F. Zhang, Y. Pu, Progress, outlook, and challenges in lead-free energy-storage ferroelectrics, Adv. Electron. Mater. 6 (2019), 1900698.
[3] X. Hao, A review on the dielectric materials for high energy-storage application, J. Adv. Dielectr. 03 (2013), 1330001.
[4] A. Chauhan, S. Patel, R. Vaish, C.R. Bowen, Materials 8 (2015) 8009–8031.
[5] F. Zhuo, D. Damjanovic, Q. Li, Y. Zhou, Y. Ji, Q. Yan, Y. Zhang, Y. Zhou, X. Chu, Giant shape memory and domain memory effects in antiferroelectric single crystals, Mater. Horiz. 6 (2019) 1699–1706.
[6] T.F. Zhang, X.X. Huang, X.G. Tang, Y.P. Jiang, Q.X. Liu, B. Lu, S.G. Lu, Enhanced electrocaloric analysis and energy-storage performance of lanthanum modified lead titanate ceramics for potential solid-state refrigeration applications, Sci. Rep. 8 (2018) 396.
[7] L. Zhang, S. Jiang, B. Fan, G. Zhang, Enhanced energy storage performance in $(Pb_{0.858}Ba_{0.1}La_{0.02}Y_{0.008})(Zr_{0.65}Sn_{0.3}Ti_{0.05})O_3$–$(Pb_{0.97}La_{0.02})(Zr_{0.9}Sn_{0.05}Ti_{0.05})O_3$ anti-ferroelectric composite ceramics by Spark Plasma Sintering, J. Alloy. Compd. 622 (2015) 162–165.
[8] C.-H. Hong, H.-P. Kim, B.-Y. Choi, H.-S. Han, J.S. Son, C.W. Ahn, W. Jo, Lead-free piezoceramics – where to move on, J. Mater. 2 (2016) 1–24.
[9] J. Li, F. Li, Z. Xu, S. Zhang, Multilayer lead-free ceramic capacitors with ultrahigh energy density and efficiency, Adv. Mater. 30 (2018), 1802155.
[10] D. Wang, Z. Fan, D. Zhou, A. Khesro, S. Murakami, A. Feteira, Q. Zhao, X. Tan, I. M. Reaney, Bismuth ferrite-based lead-free ceramics and multilayers with high recoverable energy density, J. Mater. Chem. A 6 (2018) 4133–4144.
[11] G. Wang, Z. Lu, H. Yang, H. Ji, A. Mostaed, L. Li, Y. Wei, A. Feteira, S. Sun, D. C. Sinclair, D. Wang, I.M. Reaney, Fatigue resistant lead-free multilayer ceramic capacitors with ultrahigh energy density, J. Mater. Chem. A 8 (2020) 11414–11423.
[12] G. Wang, Z. Fan, S. Murakami, Z. Lu, D.A. Hall, D.C. Sinclair, A. Feteira, X. Tan, J. L. Jones, A.K. Kleppe, D. Wang, I.M. Reaney, Origin of the large electrostrain in $BiFeO_3$-$BaTiO_3$ based lead-free ceramics, J. Mater. Chem. A 7 (2019) 21254–21263.
[13] Z. Shen, X. Wang, B. Luo, L. Li, $BaTiO_3$–$BiYbO_3$ perovskite materials for energy storage applications, J. Mater. Chem. A 3 (2015) 18146–18153.
[14] D. Fu, M. Endo, H. Taniguchi, T. Taniyama, M. Itoh, $AgNbO_3$: a lead-free material with large polarization and electromechanical response, Appl. Phys. Lett. 90 (2007), 252907.
[15] M.H. Francombe, B. Lewis, Structural and electrical properties of silver niobate and silver tantalate, Acta Crystallogr. 11 (1958) 175–178.
[16] I. Levin, V. Krayzman, J.C. Woicik, J. Karapetrova, T. Proffen, M.G. Tucker, I. M. Reaney, Structural changes underlying the diffuse dielectric response in $AgNbO_3$, Phys. Rev. B 79 (2009), 104113.
[17] L. Zhao, Q. Liu, S. Zhang, J.-F. Li, Lead-free $AgNbO_3$ anti-ferroelectric ceramics with an enhanced energy storage performance using MnO_2 modification, J. Mater. Chem. C 4 (2016) 8380–8384.
[18] N. Luo, K. Han, F. Zhuo, L. Liu, X. Chen, B. Peng, X. Wang, Q. Feng, Y. Wei, Design for high energy storage density and temperature-insensitive lead-free antiferroelectric ceramics, J. Mater. Chem. C 7 (2019) 4999–5008.
[19] J. Gao, Y. Zhang, L. Zhao, K.-Y. Lee, Q. Liu, A. Studer, M. Hinterstein, S. Zhang, J.-F. Li, Enhanced antiferroelectric phase stability in La-doped $AgNbO_3$: perspectives from the microstructure to energy storage properties, J. Mater. Chem. A 7 (2019) 2225–2232.
[20] C. Xu, Z. Fu, Z. Liu, L. Wang, S. Yan, X. Chen, F. Cao, X. Dong, G. Wang, A.C. S. Sustainable, La/Mn codoped $AgNbO_3$ lead-free antiferroelectric ceramics with large energy density and power density, Chem. Eng. 6 (2018) 16151–16159.
[21] Y. Tian, L. Jin, H. Zhang, Z. Xu, X. Wei, G. Viola, I. Abrahams, H. Yan, Phase transitions in bismuth-modified silver niobate ceramics for high power energy storage, J. Mater. Chem. A 5 (2017) 17525–17531.
[22] S. Li, H. Nie, G. Wang, C. Xu, N. Liu, M. Zhou, F. Cao, X. Dong, Significantly enhanced energy storage performance of rare-earth-modified silver niobate lead-free antiferroelectric ceramicsvialocal chemical pressure tailoring, J. Mater. Chem. C 7 (2019) 1551–1560.
[23] I. Levin, J.C. Woicik, A. Llobet, M.G. Tucker, V. Krayzman, J. Pokorny, I. M. Reaney, Displacive ordering transitions in perovskite-like $AgNb_{1/2}Ta_{1/2}O_3$, Chem. Mater. 22 (2010) 4987–4995.
[24] K. Kalantari, I. Sterianou, S. Karimi, M.C. Ferrarelli, S. Miao, D.C. Sinclair, I. M. Reaney, Ti-doping to reduce conductivity in $Bi_{0.85}Nd_{0.15}FeO_3$ ceramics, Adv. Funct. Mater. 21 (2011) 3737–3743.
[25] L. Zhao, Q. Liu, J. Gao, S. Zhang, J.F. Li, Lead-free antiferroelectric silver niobate tantalate with high energy storage performance, Adv. Mater. 29 (2017), 1701824.
[26] Y. Tian, L. Jin, Q. Hu, K. Yu, Y. Zhuang, G. Viola, I. Abrahams, Z. Xu, X. Wei, H. Yan, Phase transitions in tantalum-modified silver niobate ceramics for high power energy storage, J. Mater. Chem. A 7 (2019) 834–842.
[27] L. Zhao, J. Gao, Q. Liu, S. Zhang, J.F. Li, Silver niobate lead-free antiferroelectric ceramics: enhancing energy storage density by B-site doping, ACS Appl. Mater. Interfaces 10 (2018) 819–826.
[28] R.D. Shannon, Revised effective ionic radii and systematic studies of interatomic distances in halides and chalcogenides, Acta Crystallogr. A32 (1976) 751–767.
[29] L.L.Y. Chang, B. Phillips, Phase relations in refractory metal-oxygen systems, J. Am. Ceram. Soc. 52 (1969) 527–533.
[30] G. Wang, J. Li, X. Zhang, Z. Fan, F. Yang, A. Feteira, D. Zhou, D.C. Sinclair, T. Ma, X. Tan, D. Wang, I.M. Reaney, Ultrahigh energy storage density lead-free multilayers by controlled electrical homogeneity, Energy Environ. Sci. 12 (2019) 582–588.
[31] J. Yin, Y. Zhang, X. Lv, J. Wu, Ultrahigh energy-storage potential under low electric field in bismuth sodium titanate-based perovskite ferroelectrics, J. Mater. Chem. A 6 (2018) 9823–9832.
[32] A.A. Volkov, B.P. Gorshunov, G. Komandin, W. Fortin, G.E. Kugel, A. Kania, J. Grigas, High-frequency dielectric spectra of $AgTaO_3$-$AgNbO_3$ mixed ceramics, J. Phys. Condens. Matter. 7 (1995) 785–793.
[33] T. Shao, H. Du, H. Ma, S. Qu, J. Wang, J. Wang, X. Wei, Z. Xu, Potassium–sodium niobate based lead-free ceramics: novel electrical energy storage materials, J. Mater. Chem. A 5 (2017) 554–563.
[34] D. Wang, Z. Fan, W. Li, D. Zhou, A. Feteira, G. Wang, S. Murakami, S. Sun, Q. Zhao, X. Tan, I.M. Reaney, High Energy Storage Density and Large Strain in $Bi(Zn_{2/3}Nb_{1/3})O_3$-Doped $BiFeO_3$–$BaTiO_3$ Ceramics, ACS Appl. Energy Mater. 1 (2018) 4403–4412.
[35] Z. Yang, H. Du, S. Qu, Y. Hou, H. Ma, J. Wang, J. Wang, X. Wei, Z. Xu, Significantly enhanced recoverable energy storage density in potassium–sodium niobate-based lead free ceramics, J. Mater. Chem. A 4 (2016) 13778–13785.
[36] T. Wang, L. Jin, C. Li, Q. Hu, X. Wei, D. Lupascu, Relaxor ferroelectric $BaTiO_3$-$Bi(Mg_{2/3}Nb_{1/3})O_3$ ceramics for energy storage application, J. Am. Ceram. Soc. 98 (2015) 559–566.
[37] Q. Yuan, F. Yao, Y. Wang, R. Ma, H. Wang, Relaxor ferroelectric $0.9BaTiO_3$–$0.1Bi(Zn_{0.5}Zr_{0.5})O_3$ ceramic capacitors with high energy density and temperature stable energy storage properties, J. Mater. Chem. C 5 (2017) 9552–9558.
[38] K. Han, N. Luo, S. Mao, F. Zhuo, X. Chen, L. Liu, C. Hu, H. Zhou, X. Wang, Y. Wei, Realizing high low-electric-field energy storage performance in $AgNbO_3$ ceramics by introducing relaxor behaviour, J. Mater. 5 (2019) 597–605.
[39] J. Wu, A. Mahajan, L. Riekehr, H. Zhang, B. Yang, N. Meng, Z. Zhang, H. Yan, Perovskite $Sr_x(Bi_{1-x}Na_{0.97-x}Li_{0.03})_{0.5}TiO_3$ ceramics with polar nano regions for high power energy storage, Nano Energy 50 (2018) 723–732.

[40] D. Zheng, R. Zuo, D. Zhang, Y. Li, X. Tan, Novel $BiFeO_3$-$BaTiO_3$-$Ba(Mg_{1/3}Nb_{2/3})O_3$ lead-free relaxor ferroelectric ceramics for energy-storage capacitors, J. Am. Ceram. Soc. 98 (2015) 2692–2695.
[41] J. Wang, N. Sun, Y. Li, Q. Zhang, X. Hao, X. Chou, Effects of Mn doping on dielectric properties and energy-storage performance of $Na_{0.5}Bi_{0.5}TiO_3$ thick films, Ceram. Int. 43 (2017) 7804–7809.
[42] T. Wang, L. Jin, Y. Tian, L. Shu, Q. Hu, X. Wei, Microstructure and ferroelectric properties of Nb_2O_5-modified $BiFeO_3$-$BaTiO_3$ lead-free ceramics for energy storage, Mater. Lett. 137 (2014) 79–81.
[43] H. Qi, R. Zuo, Linear-like lead-free relaxor antiferroelectric $(Bi_{0.5}Na_{0.5})TiO_3$–$NaNbO_3$ with giant energy-storage density/efficiency and super stability against temperature and frequency, J. Mater. Chem. A 7 (2019) 3971–3978.
[44] L. Wu, X. Wang, L. Li, Lead-free $BaTiO_3$–$Bi(Zn_{2/3}Nb_{1/3})O_3$ weakly coupled relaxor ferroelectric materials for energy storage, RSC Adv. 6 (2016) 14273–14282.
[45] N. Luo, K. Han, L. Liu, B. Peng, X. Wang, C. Hu, H. Zhou, Q. Feng, X. Chen, Y. Wei, Lead-free $Ag_{1-3x}La_xNbO_3$ antiferroelectric ceramics with high-energy storage density and efficiency, J. Am. Ceram. Soc. 102 (2019) 4640–4647.
[46] Q. Zhang, H. Tong, J. Chen, Y. Lu, T. Yang, X. Yao, Y. He, High recoverable energy density over a wide temperature range in Sr modified (Pb,La)(Zr,Sn,Ti)O_3 antiferroelectric ceramics with an orthorhombic phase, Appl. Phys. Lett. 109 (2016), 262901.
[47] J. Shen, X. Wang, T. Yang, H. Wang, J. Wei, High discharge energy density and fast release speed of (Pb, La)(Zr, Sn, Ti)O_3 antiferroelectric ceramics for pulsed capacitors, J. Alloy. Compd. 721 (2017) 191–198.
[48] S. Chen, X. Wang, T. Yang, J. Wang, Composition-dependent dielectric properties and energy storage performance of (Pb,La)(Zr,Sn,Ti)O_3 antiferroelectric ceramics, J. Electroceram. 32 (2014) 307–310.
[49] Y. Bao, M. Zhou, S. Yan, F. Cao, X. Dong, G. Wang, Novel complex B-site lead oxide antiferroelectric system developed by compositional design for dielectric energy storage, J. Eur. Ceram. Soc. 39 (2019) 4785–4793.
[50] W.-B. Li, D. Zhou, R. Xu, L.-X. Pang, I.M. Reaney, $BaTiO_3$–$Bi(Li_{0.5}Ta_{0.5})O_3$, lead-free ceramics, and multilayers with high energy storage density and efficiency, ACS Appl. Energy Mater. 1 (2018) 5016–5023.
[51] Y. Pu, L. Zhang, Y. Cui, M. Chen, A.C.S. Sustainable, High energy storage density and optical transparency of microwave sintered homogeneous $(Na_{0.5}Bi_{0.5})_{(1-x)}Ba_xTi_{(1-y)}Sn_yO_3$ ceramics, Chem. Eng. 6 (2018) 6102–6109.
[52] W.-B. Li, D. Zhou, L.-X. Pang, Enhanced energy storage density by inducing defect dipoles in lead free relaxor ferroelectric $BaTiO_3$-based ceramics, Appl. Phys. Lett. 110 (2017), 132902.
[53] K. Han, N. Luo, Y. Jing, X. Wang, B. Peng, L. Liu, C. Hu, H. Zhou, Y. Wei, X. Chen, Q. Feng, Structure and energy storage performance of Ba-modified $AgNbO_3$ lead-free antiferroelectric ceramics, Ceram. Int. 45 (2019) 5559–5565.
[54] C. Cui, Y. Pu, Z. Gao, J. Wan, Y. Guo, C. Hui, Y. Wang, Y. Cui, Structure, dielectric and relaxor properties in lead-free ST-NBT ceramics for high energy storage applications, J. Alloy. Compd. 711 (2017) 319–326.
[55] W.-B. Li, D. Zhou, L.-X. Pang, R. Xu, H.-H. Guo, Novel barium titanate based capacitors with high energy density and fast discharge performance, J. Mater. Chem. A 5 (2017) 19607–19612.
[56] N. Luo, K. Han, F. Zhuo, C. Xu, G. Zhang, L. Liu, X. Chen, C. Hu, H. Zhou, Y. Wei, Aliovalent A-site engineered $AgNbO_3$ lead-free antiferroelectric ceramics toward superior energy storage density, J. Mater. Chem. A 7 (2019) 14118–14128.
[57] Y. Tian, L. Jin, H. Zhang, Z. Xu, X. Wei, E.D. Politova, S.Y. Stefanovich, N. V. Tarakina, I. Abrahams, H. Yan, High energy density in silver niobate ceramics, J. Mater. Chem. A 4 (2016) 17279–17287.
[58] L. Yang, X. Kong, Z. Cheng, S. Zhang, Ultra-high energy storage performance with mitigated polarization saturation in lead-free relaxors, J. Mater. Chem. A 7 (2019) 8573–8580.
[59] Z. Pan, D. Hu, Y. Zhang, J. Liu, B. Shen, J. Zhai, Achieving high discharge energy density and efficiency with NBT-based ceramics for application in capacitors, J. Mater. Chem. C 7 (2019) 4072–4078.
[60] B. Qu, H. Du, Z. Yang, Q. Liu, Large recoverable energy storage density and low sintering temperature in potassium-sodium niobate-based ceramics for multilayer pulsed power capacitors, J. Am. Ceram. Soc. 100 (2017) 1517–1526.
[61] D. Zheng, R. Zuo, Enhanced energy storage properties in $La(Mg_{1/2}Ti_{1/2})O_3$-modified $BiFeO_3$-$BaTiO_3$ lead-free relaxor ferroelectric ceramics within a wide temperature range, J. Eur. Ceram. Soc. 37 (2017) 413–418.
[62] F. Li, J. Zhai, B. Shen, X. Liu, H. Zeng, Simultaneously high-energy storage density and responsivity in quasi-hysteresis-free Mn-doped $Bi_{0.5}Na_{0.5}TiO_3$-$BaTiO_3$-$(Sr_{0.7}Bi_{0.2}\square_{0.1})TiO_3$ ergodic relaxor ceramics, Mater. Res. Lett. 6 (2018) 345–352.
[63] Z. Yang, F. Gao, H. Du, L. Jin, L. Yan, Q. Hu, Y. Yu, S. Qu, X. Wei, Z. Xu, Y.-J. Wang, Grain size engineered lead-free ceramics with both large energy storage density and ultrahigh mechanical properties, Nano Energy 58 (2019) 768–777.
[64] B. Qu, H. Du, Z. Yang, Q. Liu, T. Liu, Enhanced dielectric breakdown strength and energy storage density in lead-free relaxor ferroelectric ceramics prepared using transition liquid phase sintering, RSC Adv. 6 (2016) 34381–34389.
[65] H. Liu, L. Fan, S. Sun, K. Lin, Y. Ren, X. Tan, X. Xing, J. Chen, Electric-field-induced structure and domain texture evolution in $PbZrO_3$-based antiferroelectric by in-situ high-energy synchrotron X-ray diffraction, Acta Mater. 184 (2020) 41–49.
[66] Y. Chen, J. Chen, S. Yang, Y. Li, X. Gao, M. Zeng, Z. Fan, X. Gao, X. Lu, J. Liu, A bi-functional ferroelectric $Pb(Zr_{0.52}Ti_{0.48})O_3$ films: energy storage properties and ferroelectric photovoltaic effects, Mater. Res. Bull. 107 (2018) 456–461.
[67] P. Zhao, H. Wang, L. Wu, L. Chen, Z. Cai, L. Li, X. Wang, High-performance relaxor ferroelectric materials for energy storage applications, Adv. Energy Mater. 9 (2019), 1803048.